Journal of Food Engineering 156 (2015) 67–83

Contents lists available at ScienceDirect

Journal of Food Engineering

journal homepage: www.elsevier.com/locate/jfoodeng

Development of a single droplet freezing apparatus for studying crystallisation in cocoa butter droplets

Amanda M. Talhat [a], Vincent Y. Lister [a], Geoff D. Moggridge [a,*], John R. Rasburn [b], D. Ian Wilson [a]

[a] Department of Chemical Engineering and Biotechnology, University of Cambridge, New Museums Site, Pembroke Street, Cambridge CB2 3RA, UK
[b] Nestlé PTC York, Haxby Road, York YO91 1XY, UK

ARTICLE INFO

Article history:
Received 14 November 2014
Received in revised form 5 February 2015
Accepted 8 February 2015
Available online 14 February 2015

Keywords:
Cocoa butter
Polymorphism
Crystallisation
Simulation
Heat transfer

ABSTRACT

The single droplet freezing apparatus described by Pore et al. (2009), which allows crystallisation to be monitored *in situ* by X-ray diffraction, was modified to allow rapid switching of coolant gas and monitoring by video microscopy. The apparatus was used to study drops of cocoa butter undergoing simulated spray freezing at high cooling rates, *e.g.* 130 K/min. The transformation of an Ivory Coast cocoa butter to the Form V polymorph was significantly faster in drops (~40 h) than in static bulk samples (10 days) crystallised under isothermal conditions. Phase transformation was observed from Forms I/II → III → IV → melt → V, with Form V crystallising directly from the melt at 28.6 °C. Numerical simulations of the temperature evolution within the droplet established that the drops are not isothermal, explaining why nucleation was initially observed in the lower (upstream) part of the droplet.

1. Introduction

Cocoa butter is a naturally occurring, edible fat produced from the cacao bean, and is one of the major ingredients of chocolate. It consists of a mixture of triacylglycerides (TAGs) and exhibits polymorphic phase behaviour, existing in six distinct crystalline forms. These are labelled Forms I to VI following the Wille & Lutton nomenclature (Wille and Lutton, 1966) or γ, α, β' and β using the Larsson nomenclature (Larsson, 1966). Form I is the least thermodynamically stable polymorph and Form VI is the most stable. The different polymorphs can be identified via their sub-cell structure using X-ray diffraction (XRD) Clarkson et al., 1934. They can also be distinguished using differential scanning calorimetry (DSC). XRD offers unambiguous identification of the crystals present and is thus the preferred method of characterisation. Much of the chocolate literature employs the Roman classification, originally based on melting point data, and for this reason it is used here.

Real time XRD studies using laboratory X-ray diffractometers have been carried out to observe the evolving crystalline structure in cocoa butter in both static (Van Malssen et al., 1996, 1999, 1996a,b) and sheared crystallisation (Sonwai, 2002). Synchrotron XRD offers improved resolution, rapid data collection and simultaneous small (SAXS) and wide (WAXS) angle measurements, corresponding to the long and short range spacing in the crystal lattice (Macmillan et al., 2002; Macmillan and Roberts, 2002; Van Langevelde et al., 2001). In most of these studies, the cocoa butter sample is held in temperature controlled sample holder (Van Malssen et al., 1996b), a thin capillary tube (Lopez and Ollivon, 2009), or a bespoke cell (Ueno et al., 1999). The cocoa butter samples are usually heated to 50–70 °C for 15–30 min to avoid memory effects (Van Langevelde et al., 2001), and then cooled, at a rate similar to that used in DSC (*e.g.* 0.5–20 K/min), or crash cooled at 50 K/min, to the required temperature. Droplet samples of cocoa butter have not previously been studied by XRD until the development of the single droplet freezing apparatus reported by Pore et al. (2009).

The use of a droplet suspended in a flowing medium is common in heat and mass transfer studies (Fuchs, 1959). The single droplet freezing apparatus (SDFA) was developed by (Hindmarsh et al., 2007) to study temperature transitions in freezing droplets of aqueous food solutions. The SDFA allows the thermal history of a droplet to be monitored by suspending it on a fine thermocouple and subjecting it to a cold, dry air stream. This apparatus was originally used with video imaging to study the freezing behaviour of dairy solutions. SDFA devices have also been constructed for use in MRI machines for mapping emulsion creaming and solidification within droplets (Hindmarsh et al., 2004).

Gwie et al. (2006) used an SDFA to study spray-freezing of tripalmitin and cocoa butter. Their SDFA was later modified to fit into a laboratory X-ray system by Pore et al. (2009), allowing *in-situ* real time monitoring of the freezing process. It was possible to observe the transformation from Form I to the higher melting polymorphs,

* Corresponding author. Tel.: +44 1223 334 763; fax: +44 1223 334 796.
E-mail address: gdm14@cam.ac.uk (G.D. Moggridge).

http://dx.doi.org/10.1016/j.jfoodeng.2015.02.010
0260-8774/

Nomenclature

Bi	Biot number (hL/k)
c_x	percentage of phase x present (%)
C_D	drag coefficient
C_p	specific heat capacity (J/kg K)
d	droplet diameter (m)
D	duct diameter (m)
g	specific heat capacity (m/s^2)
h	average surface film heat transfer coefficient used in simulation (W/m^2 K)
h_o	surface averaged heat transfer coefficient (W/m^2 K)
H	enthalpy (J)
ΔH	enthalpy change of crystallisation, DSC testing (J/g)
I	intensity (a.u.)
k	thermal conductivity (W/m K)
K	shape factor used in Scherrer analysis (~0.9)
L	characteristic length (m)
m	mass (kg)
n	normal to boundary
Nu	Nusselt number
Pr	Prandtl number
q_{conv}	convective heat flux of droplet (W)
Q_L	latent heat released per unit gram of cocoa butter (J/g)
r	radial coordinate (m)
R	duct radius (m)
Re_{ch}	chamber Reynolds number, $Re_{ch} = \frac{Du^*}{\nu}$
Re_d	particle Reynolds number, $Re_d = \frac{Vd}{\nu}$
Re_{st}	Reynolds number, flow straightener, $Re_{st} = \frac{D_{st}u^*_{st}}{\nu}$
s	volume-weighted particle size (m)
t	time (s)
T	temperature (°C)
T_a	inlet air temperature (°C)
T_c	local temperature of the cocoa butter at the liquid/air interface (°C)
T_d	droplet temperature (°C)
T_f	mean freezing temperature measured by droplet thermocouple (°C)
T_0	initial temperature (°C)
T_s	temperature of solder in simulation (°C)
u	velocity within droplet, simulation (m/s)
u	local air velocity (m/s)
u^*	superficial air velocity (m/s)
u_d	air velocity upstream of droplet (m/s)
U	overall heat transfer coefficient (W/m^2 K)
V	terminal velocity of droplet in free fall (m/s)
w	corrected full width at half maximum (radians)
w_{obs}	observed full width at half maximum (radians)
w_s	instrumental broadening estimated using silver behenate standard (radians)

Greek symbols

θ	Bragg diffraction angle (°)
φ	polar angle (radians)
λ	wavelength (Å)
ρ	density (kg/m^3)
ν	dynamic viscosity (m^2/s)
μ	kinematic viscosity (Pa s)

Subscripts

a	air
c	cocoa butter
s	solder

Acronyms

DSC	differential scanning calorimetry
HWA	hot wire anemometer
POP	1,3-dipalmitoyl-2-oleoyl-glycerol
POS	1-palmitoyl-2-oleoyl-3-stearoyl-glycerol
SOS	1,3-distearoyl-glycerol

which were consistent with the temperature-phase transitions reported for static bulk samples crystallised under isothermal conditions by Van Malssen et al. (1999). Form V was first observed after 2 h at 24 °C, with complete transformation into Form V after 4 h; this is considerably shorter than the 1 week reported by van Malssen et al. The droplets were 2 mm in diameter, small enough to be suspended on a thermocouple junction, but large enough to interact with the X-ray beam (collimator 0.8 mm diameter).

This paper reports a substantial redesign of the X-ray SDFA to improve the consistency and accuracy of *in situ* observation of crystallisation with well-controlled temperature steps. The apparatus is able to maintain the droplet temperature at 70 °C, followed by cooling at 2–5 K/s to a temperatures as low as −10 °C. A short study of the crystallisation of a Côte d'Ivoire cocoa butter demonstrates the versatility of the device and further explores the low Biot number hypothesis proposed by Pore et al. (2009) for the rapid phase transformation in droplets. The experiments are accompanied by numerical evaluations of heat transfer with the drop to determine whether the temperature distribution within the droplets is uniform.

2. Material and methods

2.1. Apparatus

Fig. 1 shows a schematic and photograph of the SDFA. The chamber is a cylindrical Perspex duct of length 130 mm and diameter 33 mm, with air entering at the base and discharging to atmosphere at the top via 6 equally spaced 5 mm diameter holes. Chilled, dry air enters the bottom of the chamber, marked **e**, via 8 mm i.d. reinforced PVC tubing and passes through a flow straightener, marked **d**, consisting of a cylindrical duct of diameter 16.5 mm containing a honeycomb network of 3 mm diameter plastic straws.

The inlet air temperature, T_a, was measured at the entrance to the main chamber by a K-type thermocouple (marked **c**). The cocoa butter droplet was suspended from the junction of a thin K-type thermocouple, 50 μm in diameter (labelled **b**), located on the central axis 35 mm from the air inlet. The thermocouple junction has a drop of solder attached (50/50 Sn/Pb, diameter 0.9 mm), coated with nail varnish, to help droplets adhere without promoting nucleation. The thermocouple wires upstream of the droplet are encased in insulating reinforced PVC tubing of outer diameter 2 mm. The vertical position of the droplet can be adjusted. Both the inlet air temperature, T_a, and the droplet temperature, T_d, were monitored and recorded on a PC using a PicoLog data logger (Pico Technology, St. Neots, UK) at 0.25 s intervals.

The X-ray beam enters through an opening in the side wall of diameter 3 mm (**f**) and exits through an opening of diameter 10 mm (**g**) opposite; both openings are taped over with 1 mm thick Kapton© film. The chamber is mounted between the collimator and detector of the X-ray diffractometer. The spatial configuration of the X-ray system prevented the use of long entry ducts required to obtain fully developed flow patterns.

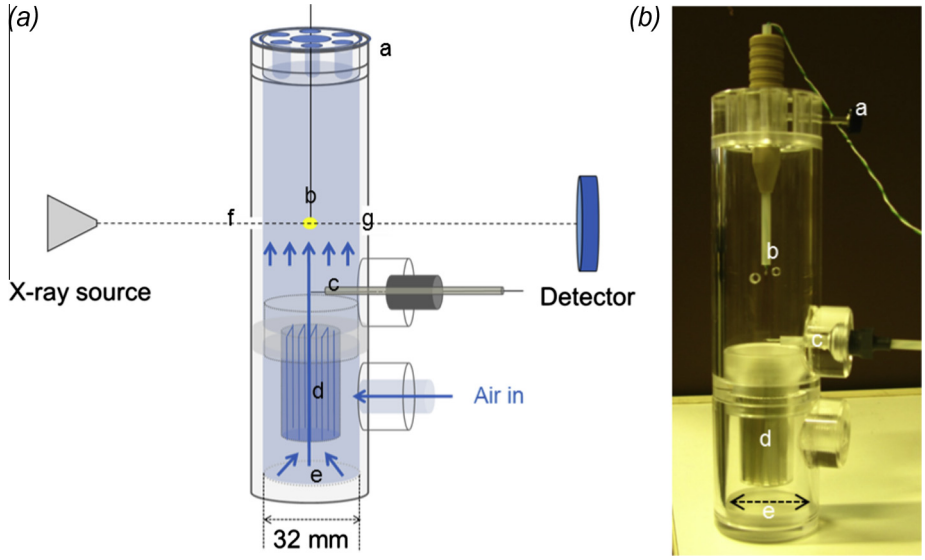

Fig. 1. (a) Schematic and (b) photograph of SDFA. Cold dry air enters the mixing chamber **e**, before passing via the flow straightener **d** into the main chamber. The air exits the cell via the holes in the droplet thermocouple holder **a**. The droplet is suspended at the junction of the thermocouple **b**. The thermocouple at **c** measures the inlet air temperature, T_a. Windows **f** and **g** allow the X-ray beam to pass through the unit.

Laboratory compressed air (1.5 bar gauge) was passed at 50 L/min from a regulator with an oil trap through a rotameter, a dehumidifier (a packed bed of anhydrous calcium chloride) and into a 8.26 m long coil of 8 mm i.d. copper tubing immersed in the refrigerant bath of a chiller unit (Cole Palmer) located underneath the X-ray chamber. The air temperature at the inlet and outlet of the chiller were monitored using K-type thermocouples. The cold, dry air passed along insulated tubing to a T-junction, where the flow was split: 30 L/min passed to the SDFA via an electronic flow controller (Omega Engineering) and the remainder was discharged to atmosphere. The air flow into the SDFA was kept below 30 L/min to prevent the droplet oscillating or being blown off. An air flow rate of 30 L/min corresponded to a superficial velocity in the SDFA chamber, u^*, of 0.58 m/s. At an inlet temperature of 0 °C, this corresponded to a mean chamber Reynolds number, Re_{ch}, of 3720. This value indicates that the flow lies in the transition region, but this is not discussed further here as the flow is unlikely to be well-developed. Hot wire anemometry (HWA) tests, detailed in Section 2.2, determined the velocity distribution around the droplet. HWA was performed at 20 °C using flow rates ranging from 20–50 L/min, as summarised in Table 1.

Droplets with diameter, d, approximately 2 mm were produced using a 1 ml syringe. The droplet thermocouple assembly was brought to a temperature of 70 °C by holding it in a channel within a heated aluminium cylinder. The droplet was held in the block at 70 °C for at least 15 min before the start of each experiment. The holding temperature and time were chosen to eliminate residual nuclei whilst minimising heat damage to the cocoa butter. After each test the thermocouple was washed with *n*-hexane to dissolve any remaining cocoa butter, rinsed with acetone, recoated with clear nail varnish and left to dry. The range of cooling rates that can be studied is determined by the air flow rate and droplet size: droplet oscillation set a limit on the maximum flow rate, while practical aspects associated with loading the drop and providing sufficient X-ray scattering set a minimum size for the drop.

Table 1
Flow rates and corresponding Reynolds numbers, calculated at 20 °C, in HWA tests to assess the velocity distribution in the SDFA chamber. Bold symbols indicate conditions used in droplet freezing tests (albeit at different air temperatures).

Flow rate (L/min)	Superficial velocity in chamber u^* (m/s)	Reynolds number in chamber Re_{ch} (–)	Reynolds number in flow straightener Re_{st} (–)
20	0.39	2480	27,600
30	**0.58**	**3720**	**41,500**
40	0.78	4960	55,300
50	0.97	6200	69,100

2.2. Local velocity measurement

The rate of heat transfer to and from the droplet is dominated by convective heat transfer and thus the air flow rate in the vicinity of the droplet. It is not practicable to employ long ducts upstream of the droplet in order to generate well developed velocity profiles owing to the confined access within the X-ray unit employed here, and heat losses to ambient. Velocity distributions were therefore measured in order to provide accurate values for the simulations reported in Section 3 and also to establish the uncertainty associated with assuming well developed flow profiles.

The velocity distribution of the air as it passed through the main chamber was determined using a hot-wire anemometer (HWA; single wire Probe type 55 P16, DANTEC Dynamics) connected via a DrDAQ data logger to a PC (Pico Technology Ltd., St. Neots, UK). The HWA element was located at the end of a 3 mm diameter rod. The probe was held vertical and measurements were made along transverse planes (labelled x and y) at two heights: the droplet level, and at the top of the chamber (marked **a** in Fig. 1). The droplet holder was not present during these measurements. Measurements were made at regular increments along each axis at both levels. The HWA probe was calibrated using a smooth, cylindrical Perspex duct of length 500 mm and diameter 33 mm with flow rates ranging from 10 to 70 L/min. All HWA tests were performed at room temperature.

The absolute velocity measurements, u, are presented in dimensionless form, *i.e.* u/u^*. Similarly, the Cartesian x and y coordinates are presented as the fractional radial position, x/R or y/R, where R is the chamber radius. The dimensionless velocity profiles are compared with the analytical result for fully developed laminar flow in a pipe and the 1/7th power law expression for turbulent flow (Incropera et al., 2007).

2.3. X-ray diffraction

XRD measurements were performed using a Bruker GADDS system employing a Cu Kα (λ = 1.541 Å) source operating at 45 kV and 45 mA. A silver behenate (AgBe) sample was used for calibration and to determine the distance from the sample to the detector. The sample was sealed in a circular disk, diameter 10 mm, with 1 mm Kapton© films on both faces, located on the centreline of the droplet freezing cell. The Bruker HISTAR 2D-detector was positioned 0.18 m from the sample at an angle of 15° off the beam axis, giving a diffraction range of approximately 0.8–30° 2θ. Exposures lasted 150 s.

2.3.1. Percentage of crystalline material present

Background subtraction was carried out using Diffrac^{Plus} EVA 10.0.0.3 (Bruker-AXS). Curve fitting was carried out in OriginPro 8.6.0 (OriginLab Corporation) using the Lorentzian function and by fixing the peak centre of the different polymorphic forms. For samples containing melt, a Gaussian fit of the broad melt peak was subtracted from the original data before any fitting. The percentage of each phase present (c_x) was estimated using

$$c_x = \frac{I_x}{I_{x,\text{pure}}} \times 100 \quad (1)$$

where I_x is the integrated intensity of Form x in each experiment, and $I_{x,\text{pure}}$ is the integrated intensity observed when the droplet is completely Form x. A mixture of Forms I and II was observed up to 22 min, Form II at 32 min, Form IV at 52 min and Form V at 2309 min. The integrated intensity for when a droplet is 100% Form x was calculated by dividing the integrated intensity of Form x at time t by the ratio of the height of the fitted peak to the height of the data peak. Where CB melt was present, its fraction was estimated by difference.

2.3.2. Crystal size

Crystals less than 1000 Å in size cause broadening of the Debye rings, and Scherrer analysis can be used to estimate the size of these crystals (Cullity, 1956), from:

$$s = \frac{K\lambda}{w\cos\theta} \quad (2)$$

where s is the mean dimension of crystalline domains in a direction normal to the reflecting planes, K is the shape factor ($K \sim 0.9$ for a sphere), θ is the Bragg diffraction angle, and w is the full-width at half maximum (FWHM) of the peak after correcting for instrumental broadening:

$$w^2 = w_{obs}^2 - w_s^2 \quad (3)$$

Here w_{obs} is the observed full-width at half maximum, w_{s} is the instrumental broadening estimated using an AgBe standard, having an average crystal size of at least 1000 Å (Huang et al., 1993). Strictly, using FWHM as the measure of broadening results, for a distribution of crystalline sizes, in s being the ratio of the root mean fourth power to the root mean square of the crystalline dimensions. The true crystalline dimension may be smaller (perhaps much smaller) than the particle dimension, if the particle is polycrystalline.

2.4. Video microscopy

Droplet freezing was recorded using a 12-bit colour QICAM video camera (QImaging, Surrey, Canada) fitted with a Leica Monozoom 7 lens (Leica Microsystems, Ontario, Canada). Video sequences were recorded using Streampix v3.16.5 (NorPix, Inc., Montreal, Canada). The images were recorded as sequence files (.seq) and then exported as both individual images (.jpeg) and a movie clip (.avi). Each image recorded was 640 × 480 pixels. The video was recorded at 2.3 frames per second. For visualisation of the solidification process, the droplet was lit by a red laser pen (wavelength 650 nm, beam diameter 1.0 mm) aligned normal to the camera, to help enhance contrast between the crystallised mass and liquid fraction. The external surface of the SDFA unit was covered with black cardboard to ensure that the laser was the only source of illumination. Image processing was performed using ImageJ (US National Institutes of Health, Bethesda, USA). Custom Montage Plugin (v1.0, Alex Watson, david.watson@nih.gov) was used to create the montage in figure.

2.5. Droplet freezing

Cold dry air was passed through the apparatus at 50 L/min until it reached steady state at the required temperature. The air was briefly diverted while the droplet was loaded and was then readmitted into the chamber at 30 L/min. The droplet started to cool during the transfer but the cooling rate increased markedly when it was exposed to air flow. The alignment of the droplet in the X-ray path was adjusted using a pre-aligned laser pen. This process took around 10 s. The laser pen was then replaced by the X-ray collimator and the first pattern recorded 2 min after the readmission of air into the unit. XRD patterns were recorded at predetermined time intervals.

The cocoa butter droplet was frozen and held at −2 °C for 20 min and then warmed to 28 °C and held at this temperature for up to 2409 min (~40 h). The recorded T_d and T_a values were smoothed using the Savitzky–Golay method (21 points, polynomial order 2) before further processing.

2.6. Materials

Cocoa butter (sourced from Ivory Coast) was supplied by Nestlé PTC York in the solid form without any additives. The free fatty acid content was determined by dissolving the cocoa butter in 95% ethanol and titrating it with aqueous sodium hydroxide as set out in AOCS Official Method Ca 5a-40; this gave 1.60 ± 0.02% as oleic acid. The triglyceride contents were analysed using high-resolution gas chromatography at Nestlé PTC York. This gave 14.6 wt.% POP, 43.4 wt.% POS and 25.3 wt.% SOS.

High-resolution gas chromatography (HR-GC) was carried out on an Agilent Technologies 6890N gas chromatograph equipped with a J&W DB17HT poly(diphenyldimethylsiloxane) column (length 30 m, internal diameter 0.25 mm, film thickness 0.15 mm) and flame ionisation detection (FID). Injection was by programmed temperature vapouriser (PTV) at 60 °C for 2 min, using helium at 14.8 ml/min and 124 + 10 kPa, followed by a temperature ramp of 300 K/min to 345 °C and holding for 4 min. High purity hydrogen was used as the carrier gas for the column, the column pressure being 124 kPa, flow-rate 1.8 ml/min and velocity 38 cm/s. The oven settings were: initial temperature, 40 °C; heating rate 50 K/min to 300 °C, 10 K/min to 340 °C and 0.2 K/min to 345 °C. The total run time was 62 min. The FID was set to a minimum peak width of 0.01 min, giving a data sampling rate of 20 Hz.

The response factors of the individual triglycerides were previously determined to lie in the range 0.7–1.4 according to analysis performed at Nestlé Research Centre (NRC) Lausanne, using a HR-GC previously calibrated with individual triglyceride standards (including POP, POS and SOS).

Samples were prepared as solutions of 10 mg of melted cocoa butter in 10 ml of high-purity hexane. For minor peaks, higher concentrations (up to approximately 10 mg/ml) were used in order to overcome baseline noise. However, in these cases, the response factors, as well as the retention times, may differ from those determined at lower concentrations. The signal intensity varied linearly

with concentration in most cases, which suggests that, at least for the minor peaks, the response factors did not change significantly at the higher concentrations employed here.

2.7. Differential scanning calorimetry (DSC)

DSC thermograms were obtained using cooling and heating rates of 20, 10 and 5 K/min using a PerkinElmer Pyris 1 power-compensated DSC (PerkinElmer Life & Analytical Sciences Inc., Boston, MA) fitted with a refrigerated intercooler. The machine was calibrated with an indium standard (5.140 mg, melting point 156.6 °C). Samples were sealed in aluminium pans (PerkinElmer Sample Pan Kit Alum 0219-0041) and loaded at room temperature. These were then heated to 70 °C and held at this temperature for 15 min, before being cooled at the selected cooling rate to −20 °C. The sample was then held at −20 °C for 1 min before being reheated to 70 °C. The onset temperature, T_{onset}, peak temperature, T_{peak}, and enthalpy change accompanying each peak, ΔH, was then estimated from each thermogram using the device software.

3. Numerical simulation of cooling of a liquid droplet

Two approaches to calculating the temperature within a cooling droplet are presented. The first is the lumped parameter model reported by Macleod et al. (2006), which is a useful tool for inspecting laboratory data. One of its assumptions is that the droplet temperature is uniform and the validity of the low Biot number condition is assessed for the droplets used in the experiments and smaller droplets which may be generated in an industrial spray freezing system. This prompted the detailed investigation of cooling within the drops described in Section 3.3.

3.1. Lumped parameter model

The droplet is assumed to be spherical and *Bi* is assumed to be small, so that the temperature distribution in the droplet is uniform. Heat losses via radiation and conduction along the thermocouple wires are ignored and the rate of convective heat loss from the surface of the droplet, q_{conv}, is given by

$$q_{conv} = \pi d^2 U (T_d - T_a) \tag{4}$$

where U is the overall heat transfer coefficient, T_a is the temperature of the cooling air, and T_d, the temperature of the droplet, is assumed to be spatially uniform, but varies with time.

Prior to nucleation (region B and D on Fig. 6) the heat loss results in a change in sensible heat and the enthalpy change can be written as

$$\frac{dH}{dt} = \frac{\pi d^3}{6} \rho C_p \frac{dT_d}{dt} \tag{5}$$

where ρ and C_p are the density and specific heat capacity of the liquid cocoa butter, respectively. Equating (4) and (5) gives

$$\frac{dT_d}{dt} = -\frac{6U}{\rho C_p d}(T_d - T_a) \tag{6}$$

which, for constant air temperature, gives

$$\ln \frac{(T_d - T_a)_t}{(T_d - T_a)_{t=0}} = -\frac{6U}{\rho C_p d} t \tag{7}$$

where t is elapsed time. The thermocouple measurements are shown to fit this general trend well in Fig. 9.

3.2. Low Biot number approximation

The Biot number is the ratio of internal (conduction) to external heat transfer resistances,

$$Bi \equiv \frac{h_0 L}{k_c} \tag{8}$$

where h_0 is the surface average external film heat transfer coefficient to the droplet, k_c the thermal conductivity of the cocoa butter, and the characteristic length L is the ratio of droplet volume to surface area (see Incropera et al. (2007)). For a sphere, $L = d/6$. *Bi* can be expressed in terms of the Nusselt number for the external heat transfer coefficient thus:

$$Bi = \frac{h_0 d}{6 k_c} = \frac{1}{6}\frac{k_a}{k_c} Nu \tag{9}$$

where k_a is the thermal conductivity of the coolant air. The ratio of thermal conductivities is approximately (see Table 2) 0.031/0.12 ≈ 0.26, say ¼. Using the Ranz and Marshall (1952) correlation to estimate *Nu*, gives

$$Bi \approx \frac{1}{6}\frac{1}{4} Nu = \frac{1}{24}\left(2.0 + 0.7 Re_d^{0.50} Pr^{0.33}\right) \approx \frac{1}{12} + 0.029 Re_d^{0.50} Pr^{0.33} \tag{10}$$

where Re_d is the Reynolds number of the sphere based on its diameter and *Pr* is the Prandtl number of the air. Eq. (10) indicates that slow moving drops will experience $Bi \sim 0.1$ and nearly isothermal internal conditions.

Identifying whether a drop is slow moving requires the terminal velocity, V, to be estimated from the weight-drag balance, *viz.*

$$\frac{\pi d^3}{6} g \Delta\rho = \frac{\pi d^2}{4} C_D \frac{\rho_a V^2}{2} \tag{11}$$

where C_D is the drag coefficient and $\Delta\rho$ is the difference in densities of the drop and air (ρ_c–ρ_a), effectively the drop density, ρ_c. It can be shown that Eq. (11) can be written as

$$\frac{4}{3} d^3 g \frac{\rho_a \Delta\rho}{\mu^2} = Re_d^2 C_D \tag{12}$$

in which the LHS has the form of a Graβoff number. Using an approximate form of the correlation of Turton and Levenspiel (1986) to estimate C_D (and acknowledging that other correlations could be used to calculate C_D)

Table 2
Physical properties of cocoa butter and solder used in heat transfer simulations.

Parameter	Value	Source
(a) Cocoa butter		
d	0.00196 m	Experimental
ρ_{liquid}	890 kg/m^3	The Manufacturing Confectioner (1969) as quoted in Beckett (2009)
ρ_{solid}	980 kg/m^3	
$C_{p,liquid}$	2220 J/kg K	Beckett (2009)
$C_{p,solid}$	2090 J/kg K	
m_s	4.1 μg	Experimental
k_c	0.12 W/m K	The Manufacture Confectioner (1991) as quoted in Beckett (2009)
(b) Solder (SnPb, 50:50)		
d	0.0009 m	Experimental
ρ	8870 kg/m^3	http://www.farnell.com/datasheets/315929.pdf
C_p	167 J/kg K	http://www.engineeringtoolbox.com/specific-heat-metal-alloys-d_153.html
k	48 W/m K	http://alasir.com/reference/solder_alloys/

$$C_D = \frac{24}{Re_d}\left(1 + .015Re_d^{0.687}\right) \tag{13}$$

yields

$$\frac{1}{18}d^3 g\frac{\rho_a \Delta\rho}{\mu^2} = Re_d + 0.15Re_d^{1.687} \tag{14}$$

Eq. (14) can be solved numerically once the droplet size and physical properties are specified. Fig. 2 shows the values of *Nu* and *Bi* calculated for cocoa butter droplets with density 890 kg m^{-3} in air (used in the simulations in Section 3.3, Table 2) at 0 °C for diameters ranging from 1 μm to 2 mm. *Bi* exceeds 0.1 when $d > 100$ μm and 0.2 when $d > 250$ μm, indicating that cocoa butter droplets generated from fine sprays would be isothermal.

For the 2 mm droplets used in the experiments reported here the terminal velocity is 6.4 m s^{-1}, which is substantially greater than the local air velocity measured in the vicinity of the droplets (Fig. 4). Fig. 2 shows that under these conditions *Bi* would be close to unity, so that the temperature conditions in the droplet would differ noticeably from those in a typical industrial spray (typically 30–300 μm). The value of *Bi* in the experiments, based on the overall heat transfer coefficient for a solder droplet *U* (see Section 4.3), was around 0.24, indicating that the experiments give a reasonable simulation of larger spray droplets. Lower air flow rates could be used in order to reduce h_0 and *Bi*, thus giving rise to temperature conditions closer to isothermal.

It should be noted that the above analysis assumes that the film heat transfer coefficient is uniform across the droplet surface. This is unlikely to the case for a falling droplet, and a spatially dependent coefficient is considered in Section 3.3. Smaller droplets will, however, give rise to fast internal conduction and the impact of non-uniformity in the external heat transfer coefficient.

3.3. Detailed simulation

The visualisation studies of the droplet undergoing freezing reported in Section 4.2 show that nucleation occurred at random in the lower part of the droplet. This indicated that the temperature in this region was lower than that around the thermocouple junction. Moreover, the heat transfer studies reported by Turton and Levenspiel (1986) and the results presented in Pore et al. (2009) indicated that the Biot number in the droplet was less than 1, but not so small (*i.e.* $Bi < 0.1$) that the temperature in the droplet can be considered uniform. Computational calculations were therefore undertaken to estimate the temperature difference across the droplet as it cooled.

The droplet and solder were modelled as two stationary spheres of different diameter located coaxially and suspended from a common point, as shown in Fig. 3. Also shown in the figure are the boundaries of three regions in the cocoa butter, encompassing 5%, 10% and 50% of the liquid volume. The surface-averaged temperature of these regions and that of the overall cocoa butter–solder assembly were calculated from the simulations as representative temperatures for comparison with the temperature measured by the droplet thermocouple, T_d, and DSC results.

3.3.1. Governing equations

Heat transfer through the liquid cocoa butter and solid solder is described by the transient heat-diffusion equation:

$$\rho C_p \frac{\partial T}{\partial t} + \rho C_p \mathbf{u}\cdot\nabla T = \nabla\cdot(k\nabla T) + Q_L \tag{15}$$

where ρ, C_p and k are the material density, specific heat capacity and thermal conductivity, respectively; T is the temperature and t time. Convection within the droplet is ignored, so that the velocity $\mathbf{u}$ is zero. Natural convection will be suppressed by the cooling of the bottom of the droplet, as well as the accompanying increase in viscosity. Conduction of heat through the thermocouple wires is also ignored. As the initial cooling stage is considered there is no enthalpy change due to crystallisation (*i.e.* $Q_L = 0$), giving:

$$\rho_s C_{p,s}\frac{\partial T_s}{\partial t} = \nabla\cdot(k_s\nabla T_s) \tag{16}$$

$$\rho_c C_{p,c}\frac{\partial T_c}{\partial t} = \nabla\cdot(k_c\nabla T_c) \tag{17}$$

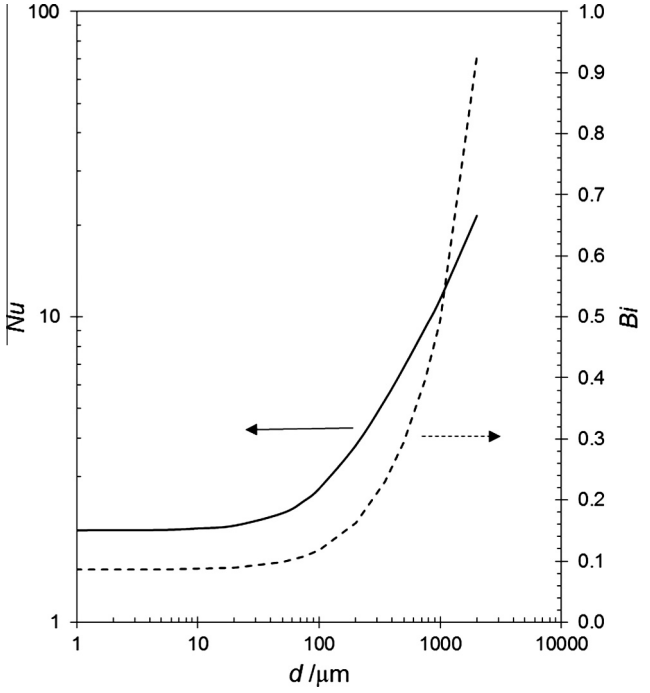

Fig. 2. Effect of diameter on estimated Nusselt and Biot numbers for cocoa butter droplet falling at terminal velocity in air at 0 °C.

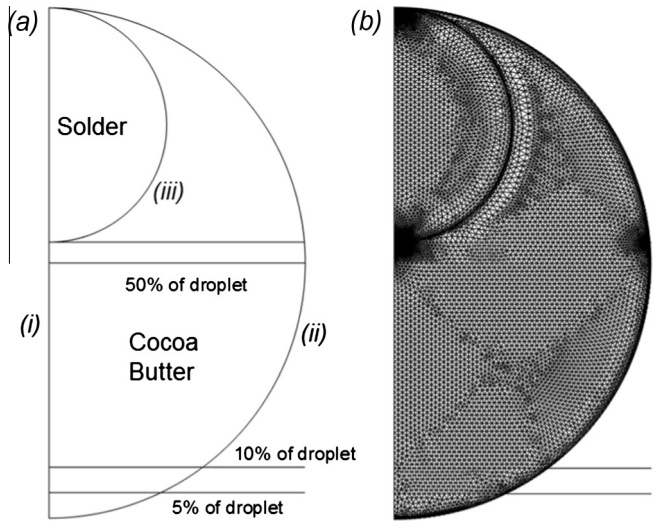

Fig. 3. Geometry in droplet cooling simulations (a) schematic showing domains and boundary labels. The horizontal lines mark sections of the droplet used in temperature averaging; (b) computational mesh with 19,911 elements, consisting of triangular and boundary layer cells. The latter (4–8 cells thick) are used on the edge of the droplet and on the solid/liquid boundary to improve the accuracy of the boundary condition calculations.

where subscripts s and c refer to the solder and cocoa butter, respectively.

3.3.2. Boundary conditions

The heat transfer conditions at the boundaries marked i–iv on Fig. 3 are:

i. Symmetry

The system is assumed to be axially symmetric about the common central axis of the spheres, so that the temperature has no dependence on the azimuthal angle. The system is then two dimensional.

ii. Convection

Heat transfer from the cooling air to the surface of the liquid droplet is described by Newton's law of cooling:

$$\mathbf{n} \cdot (-k_c \nabla T_c) = h(T_a - T_c) \tag{18}$$

where $\mathbf{n}$ is the normal to the boundary, T_a is the temperature of the air coolant, T_c is the local temperature of the liquid at the surface and h is the local film heat transfer coefficient.

The local heat transfer coefficient, h, was set to be a function of time in order to describe the two cooling phases experienced in the experiments. The droplet is initially exposed to almost quiescent ambient air for a period (approximately 12 s for the test in 6) while being transferred and loaded and is then subjected to forced convection of cooled air in the SDFA.

In the first stage the heat transfer coefficient is estimated using the result that in the limit of $Re_d \to 0$, heat transfer occurs chiefly by conduction and the average Nusselt (Nu) number is 2. This gives an estimated h value of 27 W/m^2 K for the first stage.

In the second stage, where forced convection is active, the heat transfer coefficient varies with position. The flow pattern around a single sphere in a steady air flow was computed by Hirasawa et al. (2012) and their results show a strong variation of h with the polar angle φ (Fig. 4). Their calculations were performed for a 10 mm sphere with a particle Reynolds number of 634, which is larger than that in this work ($Re_d \sim 560$). The same dependence of h on φ was utilised for this work, as shown in Fig. 4, applying a linear correction factor so that the surface averaged heat transfer coefficient (h_0) matched that measured experimentally at 61 W/m^2 K. This assumes that the flow regime is the same at that studied by Hirasawa et al.

The air temperature, T_a, changes with time. In the first stage, the air temperature is set at the lab temperature, 21.5 °C. When the cold air is admitted there is a transient in T_a and this is modelled to match the recorded values of T_a.

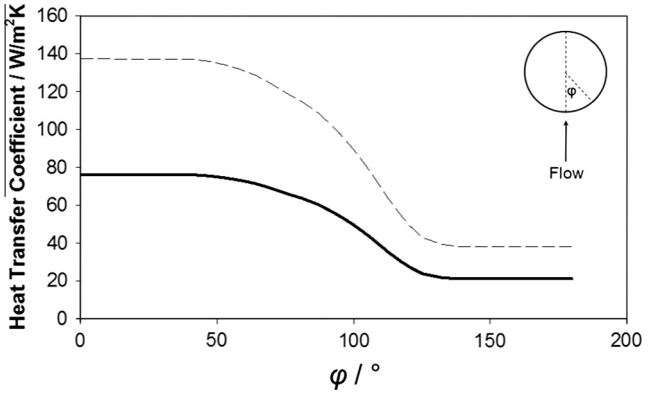

Fig. 4. Effect of polar angle φ on local heat transfer coefficient; solid locus – results reported by Hindmarsh et al. (2003) for a sphere with particle Reynolds number of 634; dashed locus – estimated for this work.

iii. Conduction at internal boundary

At the boundary between the solder and the cocoa butter the heat flux is conserved and the temperatures are equal:

$$\mathbf{n} \cdot (-k_c \nabla T_c) = \mathbf{n} \cdot (-k_s \nabla T_s) \tag{19}$$

$$T_c = T_s \tag{20}$$

3.3.3. Solution

The temperature in both domains is initially uniform at T_0 = 74 °C. The material properties are summarised in Table 2. Calculations were performed using COMSOL Multiphysics (version 4.3) which employs the finite element method to solve the above equations. Simulations were run on a PC (2.61 GHz dual core processor and 3.25 GB RAM) and typically took 10 min to converge. The mesh reported in Fig. 3 was identified by a series of trials on mesh refinement and convergence.

4. Results and discussion

4.1. SDFA velocity profile

The dimensionless air velocity profiles measured by the HWA probe for air flow rates of 20–50 L/min at the droplet plane and near the duct exit are plotted in Fig. 5. There is a noticeable region of high velocity in the centre of the duct ($-0.4 < r/R < 0.4$) at the droplet plane (Fig. 5(b)) which is less pronounced at the duct exit. Both profiles differ noticeably from the well-developed profiles for laminar or turbulent flow, although the duct exit data (5(a)) approach the 1/7th power law trend. The presence of a fast-moving central jet is expected, as the air is in the turbulent regime as it passes through the flow straightener before expanding (Table 1, $Re_{st} \sim$ 27,600 to 69,100), and it will take several duct diameters (0.029Re for laminar flow, Kay and Nedderman (1974)) to establish a fully developed flow profile. A long duct was not practicable for the SDFA owing to the restricted space available and the need to avoid heat losses (the X-ray device could not be operated in a chilled environment).

The velocity profile at the droplet plane in Fig. 5(b) shows that the velocity in the region of the droplet is locally uniform. The four different flow rates all give roughly similar profiles, with $u/u^* \sim 3$. The local velocity for the 30 L/min case is therefore $u/u^* \approx 2.5 \pm 0.1$. At 20 °C, the particle Reynolds number of the droplet, Re_d, is estimated at 560. At this Re_d value the local air flow past the droplet (if freely suspended) is expected to be unsteady with shedding of hairpin vortices in the near wake (Johnson and Patel, 1999). Heat transfer to the droplet will be dominated by forced convection in the absence of significant radiative effects and correlations such as that by Ranz and Marshall (1952) can be used to estimate the average film heat transfer coefficient. The local heat transfer coefficient is likely to vary over the droplet surface, as discussed in Section 3.

4.2. Droplet solidification

Fig. 6 shows a series of selected still images from a video of a 2 mm droplet undergoing freezing. The different stages observed during solidification, described in Table 3, are marked B–E. The droplet is initially transparent and becomes opaque as crystals, which scatter light, are formed. The red light illuminates the solder on the thermocouple junction at the top of the droplet. Reflections

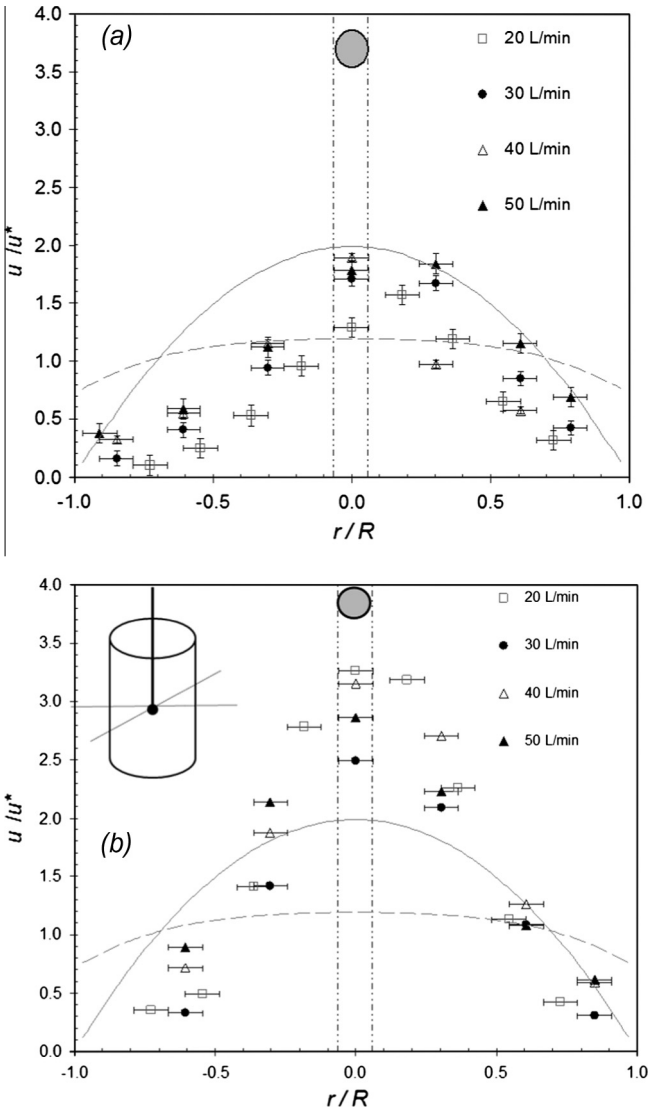

Fig. 5. Air velocity profiles at (a) chamber exit and (b) droplet level. r is the radial position from the central axis, R the radius of the duct. Data plotted as average of four measurements recorded at 90° intervals. Solid locus shows the profile for fully developed laminar flow; dashed locus 1/7th power law profile for turbulent flow. Vertical broken lines show width of 2 mm droplet.

of this red spot in the cocoa butter/air interface can be seen at the sides of the droplet at $t < 14$ s.

The droplet was initially suspended at 74 °C and the first image, $t = 0$ s, was recorded 12 s after suspension when cooling air was first admitted to the chamber (marked B). By $t = 1$ s (marked C), the air flow in the cell had stabilised. Nucleation was first observed at 4 s, with a cloud appearing at the bottom of the droplet (marked N). The solidification front slowly spread upwards through the droplet, reaching the mid-plane at 7 s and the top of the droplet at 12 s. The solder became obscured between 12 and 20 s, as the slurry of solid cocoa butter thickened. Between 20 and 40 s, there was increased scattering of red light around the droplet, due to increased condensation on the external surface of the SDFA unit.

Fig. 7 shows a droplet frozen under similar conditions to that in 6 but illuminated by a white diffuse backlight. At $t = 0$ s (marked B) the droplet was not spherical, with its shape determined by surface tension and gravity. Once cooling air was admitted into the chamber, the droplet rose. By 1 s (marked C), the air flow in the chamber had stabilised, the droplet is more spherical and the bottom of the droplet has risen. The dark ring around the droplet is due to total internal reflection of light. The droplet is not perfectly spherical in image C but these images suggest that a spherical geometry is a reasonable estimate for the heat transfer simulations.

The solidification process is characterised by the formation of small granular particles, crystallising directly from the melt. The particles sizes lie in the range of several hundred nm (hence light scattering). Due to the limited resolution of the camera (~5 μm), it was not possible to distinguish individual particles. However the changing intensity of scattered light from different layers of the droplet over time indicated that the solidification front moved both vertically upwards and radially inwards, similar to the inward freezing shell model proposed by Hindmarsh et al. (2003).

Repeated runs showed that nucleation always started at the base of the droplet, confirming that solidification did not occur via heterogeneous nucleation on the thermocouple. This indicates that the base of the droplet was always slightly colder than its centre and the region around the thermocouple junction. The assumption of a uniform temperature distribution in the droplet was not, therefore, accurate and the validity of the uniform temperature distribution estimate is examined further in Section 4.4 by comparing the experimental data with numerical simulations.

Fig. 8 is an XRD pattern for a droplet frozen under these conditions 120 s after the admission of air into the unit. There is a large peak at 21.3° and a smaller peak at 23.2° 2θ, indicative a mixture of Forms I and II. It is not possible to unambiguously determine the fraction of Forms I and II present, since the principal peak of both Forms occurs at the same angle. However Form I has a small subsidiary peak at 23.2° 2θ, so it is clear that some Form I is present in the early stages of crystallisation and that this decreases in favour of Form II with time. No XRD patterns giving definitive evidence of Form I crystallising alone were recorded in these experiments so these two polymorphs are not separated in Figs. 14 and 15. Scherrer analysis indicates the crystal dimensions were 130 ± 10 Å perpendicular to the planes responsible for the 21.3° reflection.

4.3. Heat transfer aspects

Fig. 9 shows the evolution of temperature of a cocoa butter droplet, initially at 74 °C, exposed to cold air at 0 °C (as in Fig. 6). There was a 20 K reduction in temperature as the droplet was transferred to the SDFA and the X-ray beam aligned (between A and B). The cold air flow was restarted at B, accompanied by a noticeable change in the droplet cooling rate (see T_d) and air temperature (T_a). The latter reached steady state value at C, after about 15 s. There was a discontinuity in the T_d profile, marked D, at $T_d = 19.7$ °C, marking the detection of solidification. This discontinuity is more evident in Fig. 9(b). The cooling rate in the droplet between B and D was 3.0 K/s. Although the thermocouple first detected the phase change at D in Fig. 9, the corresponding still image in Fig. 6 indicates that a proportion of the lower half of the droplet had already solidified by this point. This indicates that the assumption of a uniform internal temperature distribution was not accurate.

4.3.1. Uniformity of temperature distribution in droplet

Crystallisation in the droplet was accompanied by an almost linear decrease in T_d between D and D*, with a cooling rate of 0.62 K/s. The reduction in cooling rate relative to that during the period B–D was due to the release of latent heat of crystallisation. After D* the temperature decays in an exponential fashion and approaches T_a asymptotically. This region corresponds to the cooling of the solidified droplet and gives a roughly linear trend in Fig. 9(b).

The data from Fig. 9(a) are plotted in the form suggested by Eq. (13) in Fig. 9(b). Linear regions are evident at: (*i*) AB – corresponding

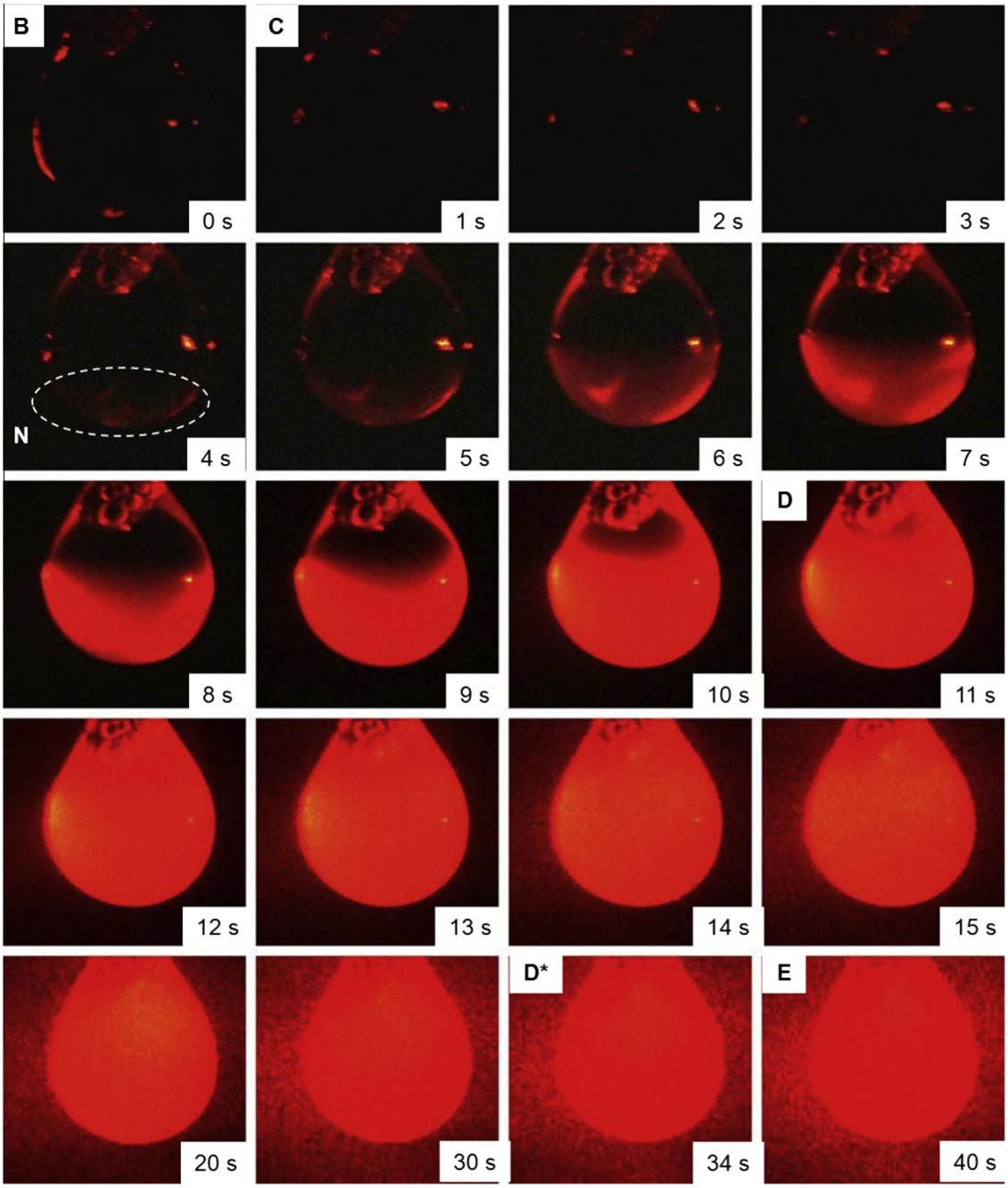

Fig. 6. Video stills showing the freezing of a 2 mm diameter droplet of Ivory Coast cocoa butter. The droplet was frozen at T_a = 0 °C and maintained at this temperature for 40 s. The t = 0 s image corresponds to when air is readmitted into the unit (B). Nucleation, labelled N, is first observed 4 s after B. The solidification front moves upwards and inwards and the droplet appears to be fully solidified by 20 s. Labels B–E correspond to different stages of the freezing process labelled in Fig. 8 and Table 3.

Table 3
Stages in droplet freezing (Figs. 6 and 8).

Stages of freezing	Description
O–A	Suspension of droplet on thermocouple
A–B	Transfer of thermocouple to SDFA channel
B	Readmission of air into SDFA channel
C	Air flow in SDFA channel stabilises
B–D	Cooling of liquid CB
N	Nucleation first observed in droplet
D–D*	Solidification of CB
D*–F	Cooling of solid CB
E	Fully solidified droplet as indicated by microscopy test

to heat loss by natural convection during droplet transfer; (*ii*) BD – air cooling of the liquid droplet; and (*iii*) D*F – air cooling of solidified droplet. The region DD* – corresponding to CB solidification – is not linear in Fig. 8(b), as expected due to the release of latent heat. During AB, the inlet air is diverted away from the SDFA unit, which leads to the unit warming up due to natural convection within the X-ray cabinet (T_a = 4.2 °C). During BD, T_a decays exponentially from 4.2 to 0 °C, as the SDFA unit is cooled along with the liquid CB droplet. The value of U obtained for the droplet in region BD in Fig. 9(b) is 60.7 ± 1.2 W/m^2 K. Parameters used in calculating this value are summarised in Table 2.

The Biot number is now estimated. An average heat transfer coefficient, h, of 89 W/m^2 K was obtained from similar tests using

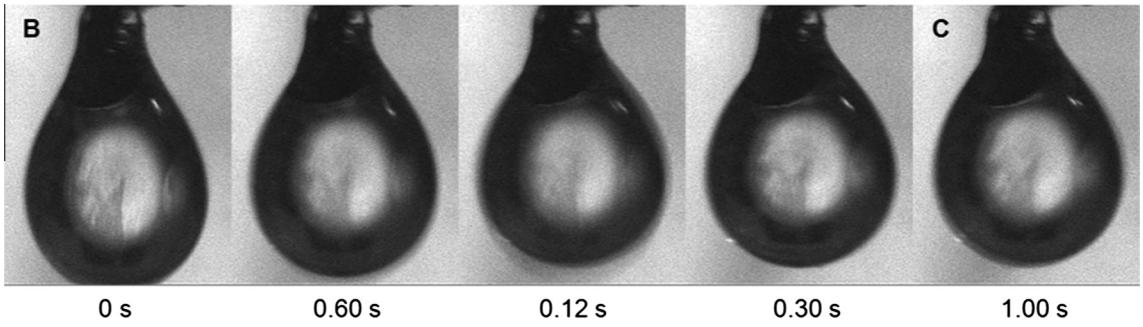

Fig. 7. Droplet displacement after cooling air is admitted to the chamber at $t = 0$ s. The droplet was frozen under similar conditions ($T_a = 0$ °C) to the droplet in Fig. 5. The droplet was lit from behind with the light directed through the droplet. Labels B and C correspond to the different stages of freezing in Table 3.

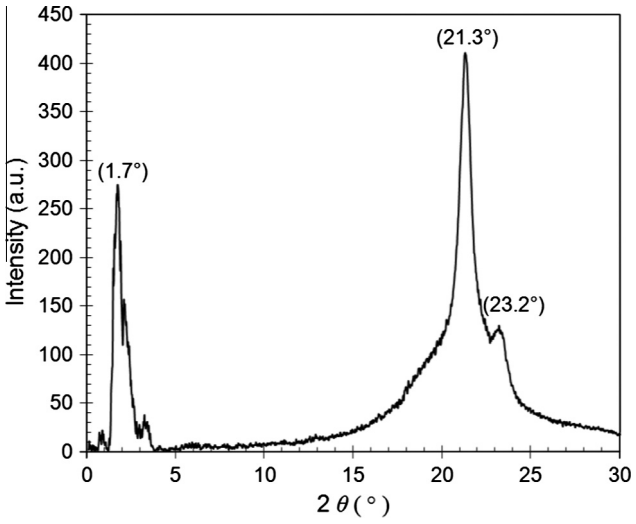

Fig. 8. X-ray diffraction pattern of a frozen droplet ($T_a \sim 0.5$ °C, similar condition to the droplet in Fig. 5) taken 120 s after B. Peaks indicate the crystals are a mixture of Forms I and II.

a thermocouple with a 2 mm drop of solder attached. The thermal conductivity of solder is 40 times higher than CB so these measurements are effectively free of internal heat transfer resistance and thus should give a good approximation of the true external heat transfer coefficient in the CB droplet experiments. Comparing this value to the overall heat transfer coefficient above indicates that external heat transfer presents the largest resistance. *Bi* is then ~0.24 for the tests reported here, indicating that the internal temperature distribution is expected to be close to, but not completely, uniform.

4.3.2. Simulated temperature profiles

The validity of this near-uniform temperature approximation is examined by simulation. Fig. 10 presents results from simulations compared with the experimentally measured droplet temperature, T_d. In the simulations the droplet is initially isothermal at 74 °C (marked A). The droplet then undergoes heat loss via natural convection until $t = 12$ s, which corresponds to the droplet transfer stage (AB) in Fig. 9. At B, cooling air is readmitted to the chamber, which leads to rapid cooling of the droplet. N marks when nucleation is first observed and D when the thermocouple first detects the phase change.

Fig. 10(a) shows good agreement between the measured droplet temperature profile, T_d, and the simulated temperature at the thermocouple. There is good agreement until around $t = 23$ s, after which time T_d deviates from the simulated thermocouple temperature due to the evolution of latent heat of crystallisation. Fig. 10(b) shows the temperature profiles for the different volumes of the droplet identified in Fig. 3, alongside the results from the simulation. The material at the bottom of the droplet cools more quickly than that near the thermocouple, which explains why nucleation is observed in this region in Fig. 6 before it is detected in the temperature measurement. The simulations show that there is a significant temperature difference between the droplet temperature measured at the thermocouple junction (T_d) and the lower regions of the cocoa butter droplet (5–50% volume sections). It is clear that the internal temperature distribution of the droplet cannot be assumed to be uniform and care must then be taken in attributing changes to measured temperatures.

The images in Fig. 6 indicate that nucleation occurs at the surface of the droplet, where the CB experiences low temperatures first. The surface average temperatures were evaluated for the regions marked in Fig. 3 (*e.g.* the 5% value is the average temperature of the region enclosing 5% of the droplet liquid volume) and are plotted in Fig. 10(b). The 5% and 10% values are similar and are noticeably colder than the bulk average and measured values.

The difference in predicted temperature between the solder and the different surface averaged sections is plotted in Fig. 10(*c*), with the largest temperature difference, ΔT, arising at the base of the droplet (5% volume section). ΔT increases rapidly for 3 s after time B, when cooling air is readmitted to the chamber, and after 4 s slowly decreases. At B, there is a difference of 2.5 K between the thermocouple and the bottom of the droplet. This increases to 16 K at $t = 15$–16 s, when nucleation is first observed in Fig. 6 (image N), corresponding to an average surface temperature in the 5% region of 25 °C. The simulation continues to give a good description of T_d for another 7 s, indicating the amount of latent heat evolved is small. When solidification is first manifested in the T_d profile (at D, $t = 23$ s) ΔT is 8.8 K and the droplet thermocouple measures 19.2 °C.

4.3.3. Latent heat effects

Latent heat of crystallisation is released in the region between D and D* on Fig. 9, reducing the cooling rate within the droplet. The rate of change in T_d can be related to the difference between the rate of latent heat release, Q_L, and the rate of heat transfer by convection from the droplet surface. Assuming again that the droplet is spherical with uniform temperature, an energy balance gives

$$\frac{\pi d^3}{6}\rho C_p \frac{dT_d}{dt} = \frac{\pi d^3}{6}\rho Q_L - \pi d^2 U(T_d - T_a) \tag{21}$$

U is known so Q_L can be estimated at each time interval between D and D*. This lumped parameter approach will give an estimate of Q_L and would require considerable refinement in order to calculate the latent heat.

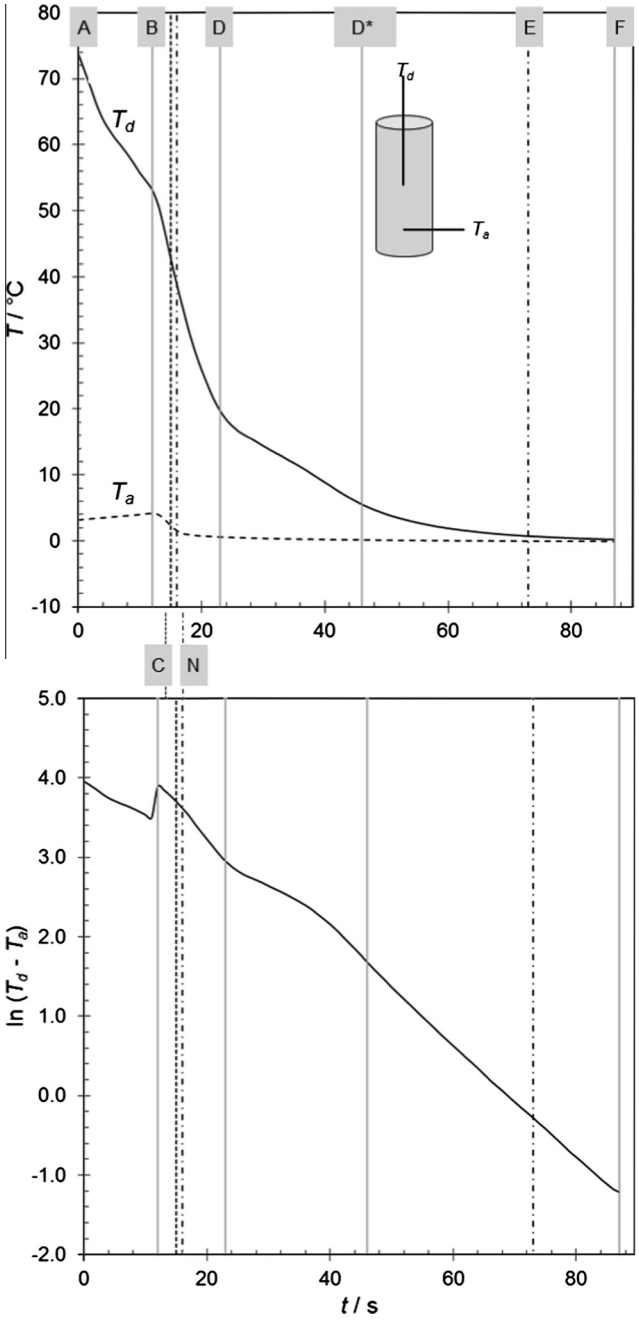

Fig. 9. Temperature evolution during droplet freezing: (a) measured air and droplet temperatures; (b) data in (a) plotted in the form of Eq. (7). Conditions are those in Fig. 6: air flow rate 30 L/min, T_a = 0 °C. Labels described in Table 3.

The results obtained for the data set in Fig. 9 are presented in Fig. 11. Two regions are evident in the temperature sweep (Fig. 11(b)):

(i) The region between 53 and 74 °C corresponds to the region AB in Fig. 9. The high Q_L values are an artefact resulting from the droplet undergoing slow cooling before the readmission of the air into the unit. This is caused by natural convection and gives rise to a lower U value; inspection of Eq. (20) shows that this will result in an erroneous, positive, estimate of Q_L. This region is not considered further.

(ii) There is a broad peak centred at T_d = 19 °C corresponding to latent heat released from crystallisation which corresponds to the region DD* in Fig. 9. The peak is not symmetrical, increasing sharply at first, which matches the appearance of crystals in Fig. 6. Integrating across this region yields an estimate of the latent heat of crystallisation to be 18.1 ± 0.01 J/g.

4.4. DSC

DSC thermograms for the batch of Ivory Coast cocoa butter used in the droplet freezing experiments are reported in Fig. 12. The cocoa butter was initially heated to 70 °C to eliminate any residual Form V/VI nuclei then cooled to 20 °C at a set cooling rate. Different samples were used for each cooling rate. Fig. 12(a) shows that cooling gave a large exothermic peak (corresponding to Form II) centred at 5.1, 4.0 and 2.6 °C for a cooling rate of 5, 10 and 20 K/min, respectively, followed by a smaller exothermic shoulder peak (attributed to Form I) at around −5 °C. The observed two exothermic peaks for the cooling rates used is consistent with that reported by Van Malssen et al. (1996a) that at cooling rates greater than 2 K/min Form II crystallises first followed by Form I. The decrease in the onset temperature of solidification with increasing cooling rate is also consistent with that reported in literature (Spigno et al., 2001; Fessas et al., 2005). The samples were then maintained at −20 °C for 1 min before being reheated to 70 °C at the same rate. Fig. 12(b) shows a small endothermic peak corresponding to melting of Form I crystals around 0 °C followed by a large endothermic peak (Form II) centred at 9.5, 10.0 and 11.8 °C for 5, 10 and 20 K/min, respectively. The shoulder on this large endothermic peak, around 17 °C, corresponds to the melting of Form III crystals.

The enthalpy of crystallisation associated with Form II crystal formation was evaluated at 42.4, 38.7 and 37.0 J/g at cooling rates of 5, 10 and 20 K/min respectively. These values are smaller than the 86.2 J/g reported by Fessas et al. (2005) for pure Form II for cooling at 2 K/min and 88.7 J/g by Schlichter Aronhime et al. (1988) for cooling at 0.3 K/min. An alternative explanation is that approximately half the cocoa butter crystallises as Form II. These values are all considerably larger than those obtained by the temperature transient analysis in Section 4.3.

A discrepancy is expected as the transient analysis involves several estimated values, *e.g.* C_p, ρ, and U. A significant source of error arises from the assumption that the droplet internal temperature distribution is uniform. An alternative method for estimating the latent heat of crystallisation in the droplet would be to extend the simulation to include crystallisation and cooling of the solidified droplet. Tanner (2011) reported simulations of this nature. An inward freezing shell model was used to describe crystallisation and gave a good description of the T_d–t profiles reported by Gwie et al. (2006). The video microscopy results here, however, suggest that an inward freezing shell model is not an accurate description of the process. An alternative approach would be to use a phase field model of the solidification which could account for the evolving liquid–solid interface as well as development of crystal microstructure in the final solid (Galloway and Smyth, 1997).

Before such complex simulations are performed, however, the length scale of interest needs to be considered. Industrial spray drying and freezing devices use considerably smaller droplets than those employed in this study, which can result in smaller Biot numbers, and droplet rotation is likely to occur. There are noticeable differences between the temperatures at which the onset of cooling is observed in the DSC tests, (8–10 °C) and the temperatures where nucleation is observed in the droplet tests. Surface nucleation (point N on Fig. 10) occurred at an estimated surface temperature of 25 °C, while nucleation in the bulk, as indicated by the thermocouple transient (point D on Fig. 10), corresponded to T_d = 19.3 °C. Neither of these values corresponds to the DSC value, although the 5% surface average temperature had reached 10.5 °C by point D. This discrepancy is further confounded by the

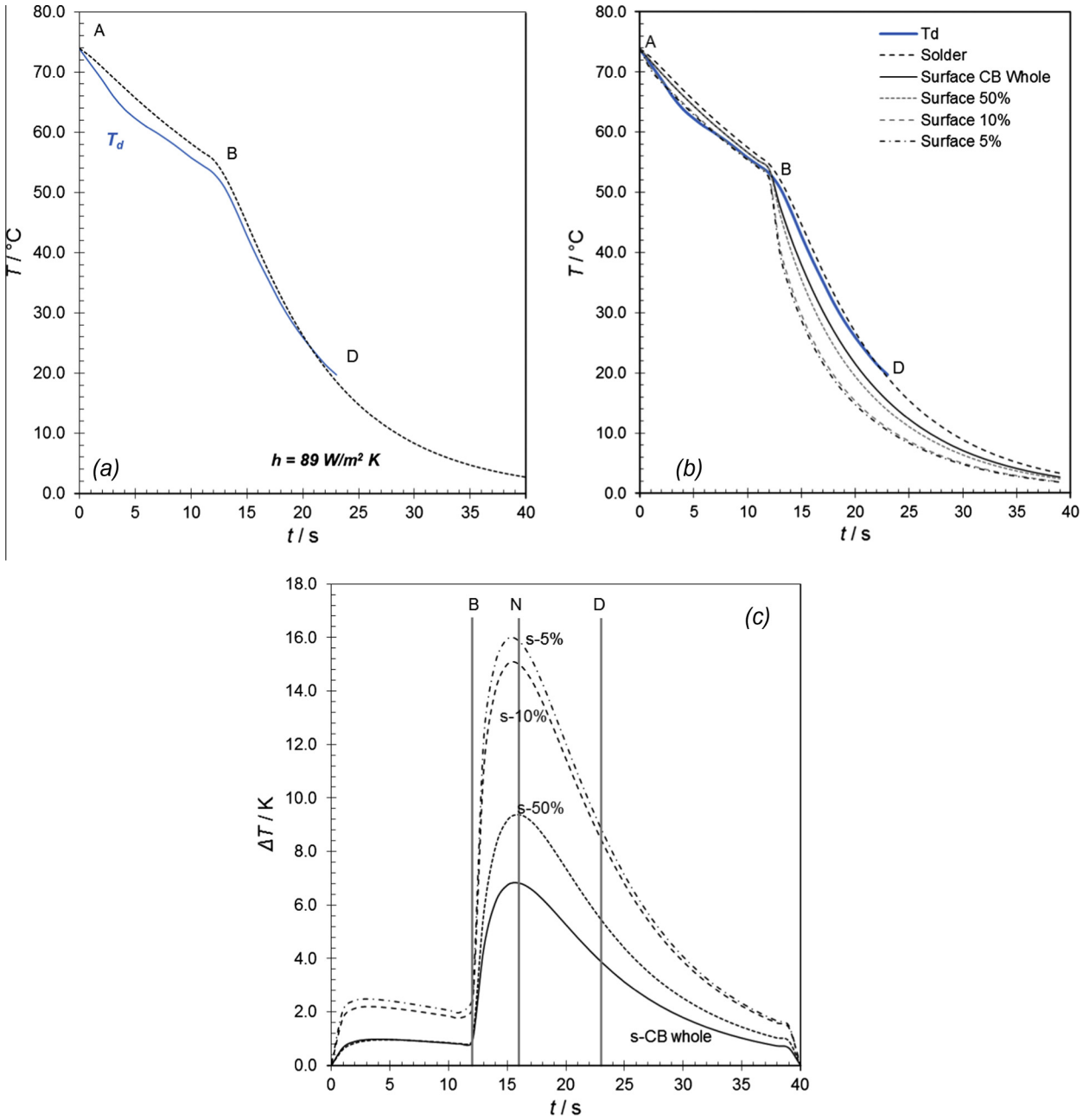

Fig. 10. Comparison of experimental temperature evolution in a droplet with simulations: (a) solder temperature profile for average heat transfer coefficient, h = 89 W/m^2 K (dotted, black locus), and measured droplet temperature, T_d, (bold, blue locus); (b) overall temperature profiles for the surface of the different regions marked on Fig. 3 and T_d; (c) temperature difference between the solder and the surface of the different sections as shown in Fig. 3; labels A, B, N and D correspond to those shown in Fig. 9. (For interpretation of the references to colour in this figure legend, the reader is referred to the web version of this article.)

difference in cooling rates: there is a noticeable shift in the DSC cooling profiles to the left with increasing cooling rate, shifting the onset of nucleation to lower temperatures. The cooling rate in the droplets is significantly greater than in the DSC tests, at 180 K/min, so one would expect the onset of nucleation to be shifted to colder temperatures (Spigno et al., 2001). The temperatures at which nucleation is observed in the droplet are higher than the melting temperature of Form I (5 °C) and close to the melting temperature of Forms II (20 °C) and III (23 °C). The XRD spectra indicate that the initial crystals formed consist of Forms I and II. Fig. 11(b) indicates that a significant fraction of the latent heat is released when the surface temperature is below 5 °C (although the bulk temperature is considerably higher). Thus it is plausible that regions of the droplet are below the melting point of Form I (and so initially crystallise into this Form), even though the bulk temperature is too high to allow the formation of Form I. This would explain the X-ray observation of initial formation of a mixture of Forms I and II, followed by gradual transformation into pure Form II.

4.5. Polymorphic phase transitions in droplet

4.5.1. Forms I to V transition

Fig. 13 shows a series of XRD spectra for a cocoa butter droplet, frozen and held at −2 °C for 20 min before being gradually warmed (over approximately 11 h) to 28 °C, and held near, this temperature until 2309 min (~38 h). The air temperature dropped to around 25 °C after 1000 min due to overnight changes in ambient

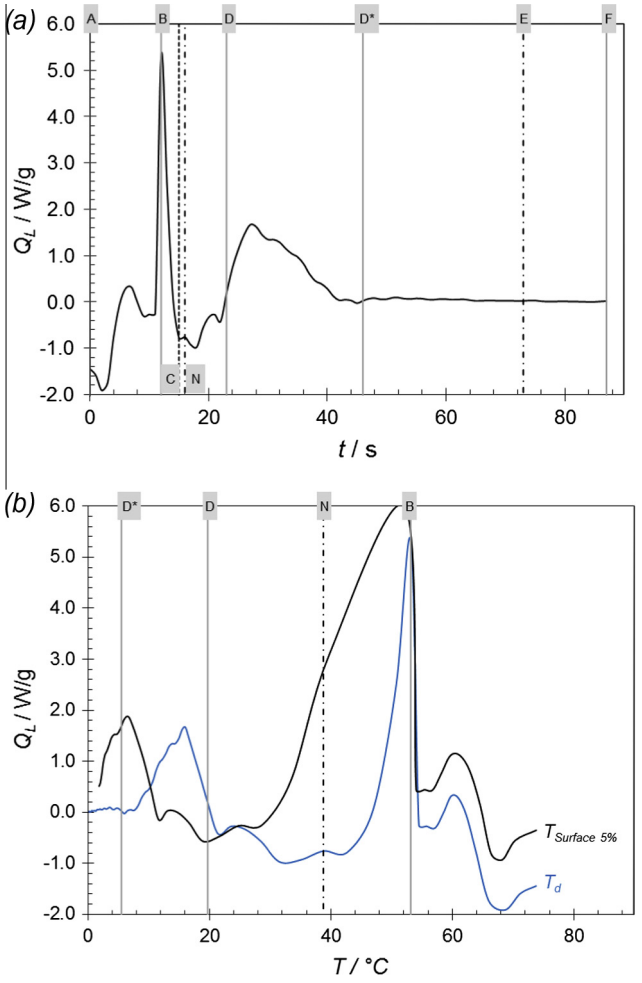

Fig. 11. Estimated latent heat release rate, Q_L, for the droplet in Fig. 8 plotted as a function of (a) time and (b) temperature. In (b), the blue locus shows Q_L plotted against the measured droplet temperature, T_d, and the black locus, the surface of the bottom apex (5%) of the droplet, $T_{Surface\ 5\%}$. labels A to F are explained in Table 3. (For interpretation of the references to colour in this figure legend, the reader is referred to the web version of this article.)

temperature. Fig. 8 shows that the droplet temperature reaches T_a within 90 s so the latter value is quoted. After 2 min ($T_d \sim T_a$ = −2.0 °C), the wide angle region (WAXS) exhibited two peaks at 21.1° and 23.0° 2θ, which are characteristic of Form I. The small angle region (SAXS) shows three peaks at 1.7°, 2.5° and 3.1° 2θ which also indicate Form I. The droplet was maintained at −2.0 °C for a further 20 min, over which time the intensity of the shoulder peak at 23.0° decreased whilst the intensity of the peak at 21.1° increased. Over this time the triplet in the SAXS region transforms into a doublet with peaks at 1.9° and 2.0° 2θ by 22 min. These changes can be explained by the droplet containing a mixture of Forms I and II. Form II exhibits a single peak in the WAXS region, also at 21.0°, which overlaps the peak for Form I and making it difficult to identify whether the sample is purely Form I or a mixture of Forms I and II from WAXS data only. Thus growth of the 21.1° peak (Forms I and II) whilst the 23.0° peak (Form I) decreases in intensity suggests transformation of Forms I to II; the shift of the 1.7° (Form I) peak to 1.9° (Forms I and II) is possible if there is an increase in Form II which will exhibit a peak at 1.8° 2θ as shown at 32 min.

After 32 min the air had warmed to −0.8 °C and was accompanied by the complete loss of the shoulder peak at 23.0° 2θ and the migration of the principal peak from 21.1 to 21.0° 2θ. This suggests that the droplet has completely transformed into Form II.

As the inlet air was warmed further (42 min, T_a = 18.5 °C), the principal peak shifted to 20.9° 2θ, and broad shoulders were formed either side of the peak at around 19° and 22.5°. The single sharp SAXS peak at 1.8° 2θ indicates that the droplet is mostly Form II, and the shoulder peaks at 19° (melt) had 22.5° indicate transformation into Form III/IV. The appearance of the melt peak at 19° means that the Forms II to III/IV transformation proceeds via partial melting of Form II, this is in comparison to the rapid and complete transformation of Forms I to II which is a solid state transition (D'Souza et al., 1990).

By 52 min the air had warmed to 22.8 °C, and the WAXS region shows peaks at 20.9° and 20.2° 2θ characteristic of Form IV, and a broad peak indicative of the melt centred at 19°. The SAXS region showed a single peak at 1.9° 2θ. This indicates that the droplet has transformed into Form IV, with some melt also present. By the time air reached 25.6 °C (62 min), the broad peak in the WAXS region remains which is characteristic of the melt. A small peak, attributed to Form IV, is evident at 20.2° 2θ. The 1.9° peak in the SAXS region was also present at much reduced intensity. Between 62 and 662 min, the droplet was warmed to 28.5 °C and the 1.9° 2θ peak of Form IV disappeared. This is consistent with completion of droplet melting.

Crystallisation from the melt is evident after 707 min with the emergence of a peak at 19.2° 2θ. No peaks were observed in the

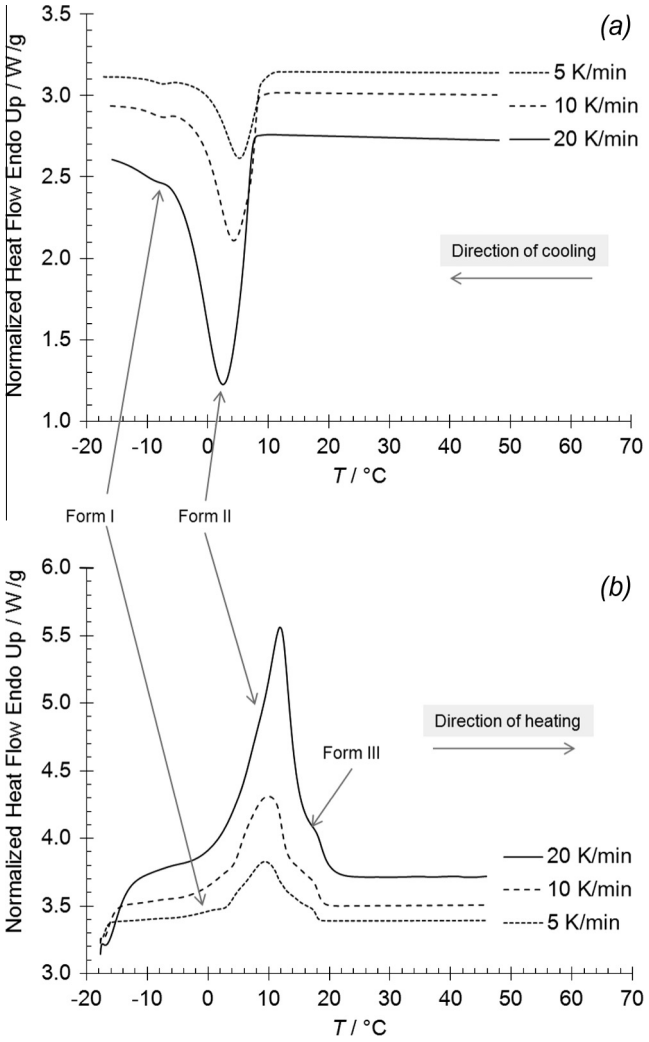

Fig. 12. DSC thermograms of Ivory Coast cocoa butter (a) cooled from 70 °C to −20 °C, and (b) heated from −20 °C to 70 °C after 1 min at −20 °C.

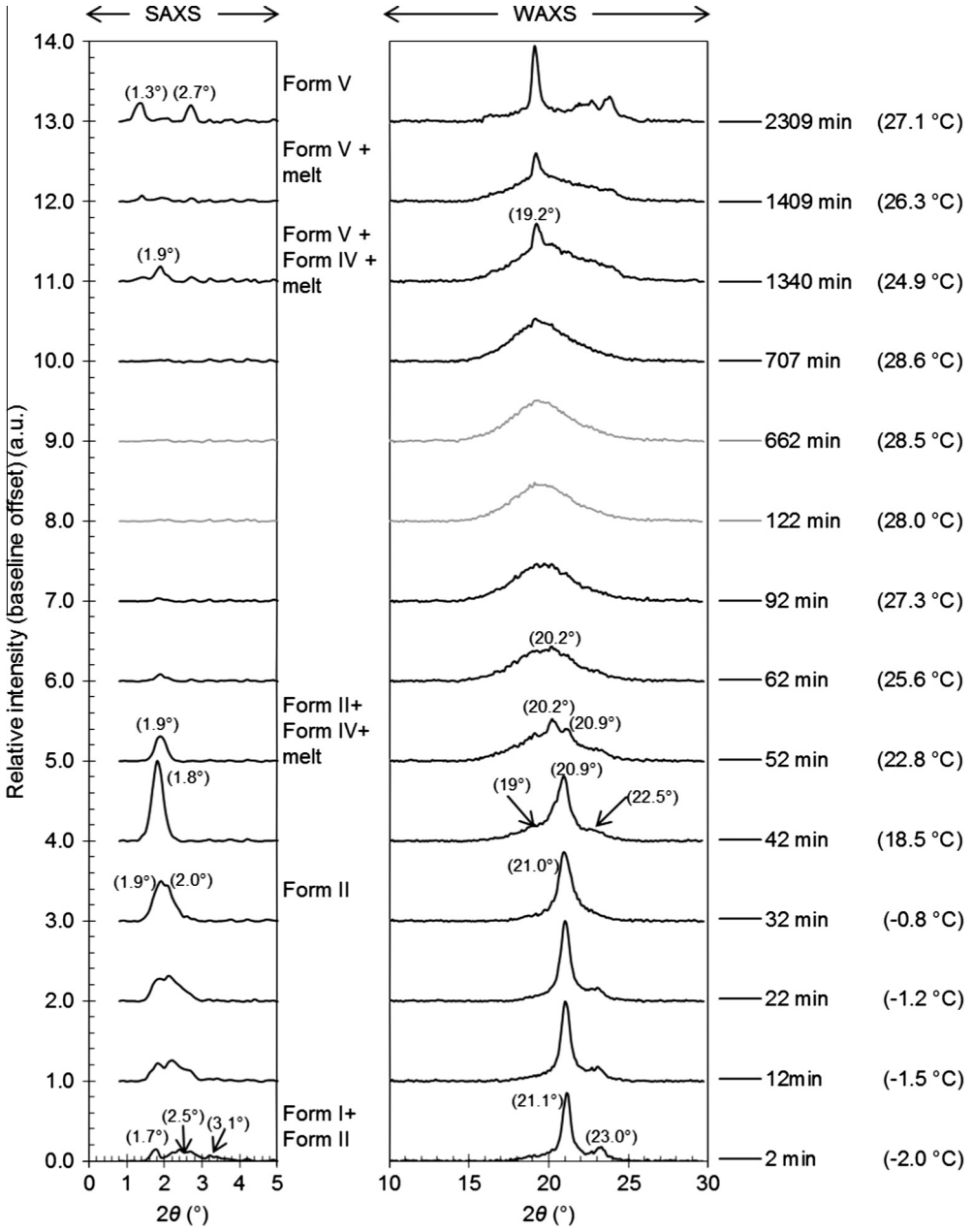

Fig. 13. XRD spectra showing evolution of polymorphs. The SAXS peaks are relative to the intensity recorded for the 1.8° peak at 42 min (I = 2250 Counts), the WAXS peaks are relative to the intensity of the 21.1° peak at 22 min (I = 4954 Counts) Time elapsed since readmission of cooling air into the chamber and T_a ($\sim T_d$) shown on the right. Peaks have been labelled in bracket to help differentiate between the different forms which are also labelled. Grey loci indicate molten cocoa butter.

SAXS region at this point. By 1340 min, the air temperature had decreased to 24.9 °C. The WAXS peak at 19.2° 2θ became more intense and the SAXS region showed 3 peaks at 1.3°, 1.9° and 2.7°, with 1.9° being the most intense. The 1.3° and 2.7° doublet indicated that Form V was present, and the 1.9° peak Form IV. The air had warmed up by 1409 min to 26.3 °C, at which point the 1.9° 2θ peak was reduced in intensity, suggesting partial Form IV melting in the range 24.9 °C to 26.3 °C.

4.5.2. Percentage of crystalline material present

The quantity and average particle size of the polymorphs present in each diffraction pattern was estimated from the integrated intensity and full-width at half maximum of the principal peak. The percentage of each Form present is plotted against (a) time, and (b) droplet temperature (measured at the thermocouple) in Fig. 13. Forms I and II were both formed initially (74%) and the fraction increased with time, reaching 97% after 20 min. This was accompanied by transformation into Form II at 100% after 32 min. By 42 min, the droplet was largely Form II (82%), followed by a partial transformation into Form IV (48%) after 52 min. The melting of Form IV (62 min, 22%) was accompanied by an increase in the amount of melt present. Form V was subsequently formed directly from the melt at 707 min (13%). However, crystallisation of Form V was slow, reaching 36% at 1409 min and 87% at 2309 min. At 1390 min, both Form IV (SAXS) and V (WAXS) are observed, which is estimated to be at 25% and 46% respectively. The 46% value is likely an overestimate due to overlapping Forms IV and V peaks in the WAXS region, and is confirmed as the Form V percentage drops to 36% by 1409 min. Overall the transformation into Form V was quite rapid similar to that reported by Pore et al.

(2009) which is significantly shorter than the 1 week reported for isothermal crystallisation of Form V in the literature (Van Malssen et al., 1999).

The spectra and percentage of each form present indicate that the transformation from Forms I to II is rapid and occurs via solid-state transitions, while those from Forms II to IV to V are much slower and involve melting. Inspection of Figs. 13 and 14(b) indicates that Form V was formed first from the melt, and that the occurrence of Form IV at 1390 min was due to the air temperature dropping to 25 °C. The particle sizes were estimated from Scherrer analysis of the XRD peaks. The Forms IV and V crystals could not be estimated using this method as the full-width at half maximum of the Form V peak was similar to that that of the AgBe standard: it can be inferred that these crystals were at least a few hundred Å. Crystals responsible for the peak at 21.1° (Forms I and II) between 2 and 22 min were on average 300 Å in size, with the 23.0° peak associated with Form I crystals corresponding to a size of 120 Å. The peak at 21.0° (Form II) at 32 min corresponded to an average size of 110 Å.

4.5.3. Thermal trajectory

The results are now presented in the form of the isothermal phase transition scheme which Van Malssen et al. (1999) used to describe the evolution of polymorphic forms for a Cameroon cocoa butter. Their samples were heated to 60 °C for 60 s, cooled to the required temperature over 120 s, and then held at that temperature until crystallisation was observed. The samples consisted of 150 mg CB in holders, 10 × 15 × 1 mm in dimension, and were subject to XRD analysis. The polymorphs present were plotted in *T*–*t* space and approximate boundaries to each polymorphic region

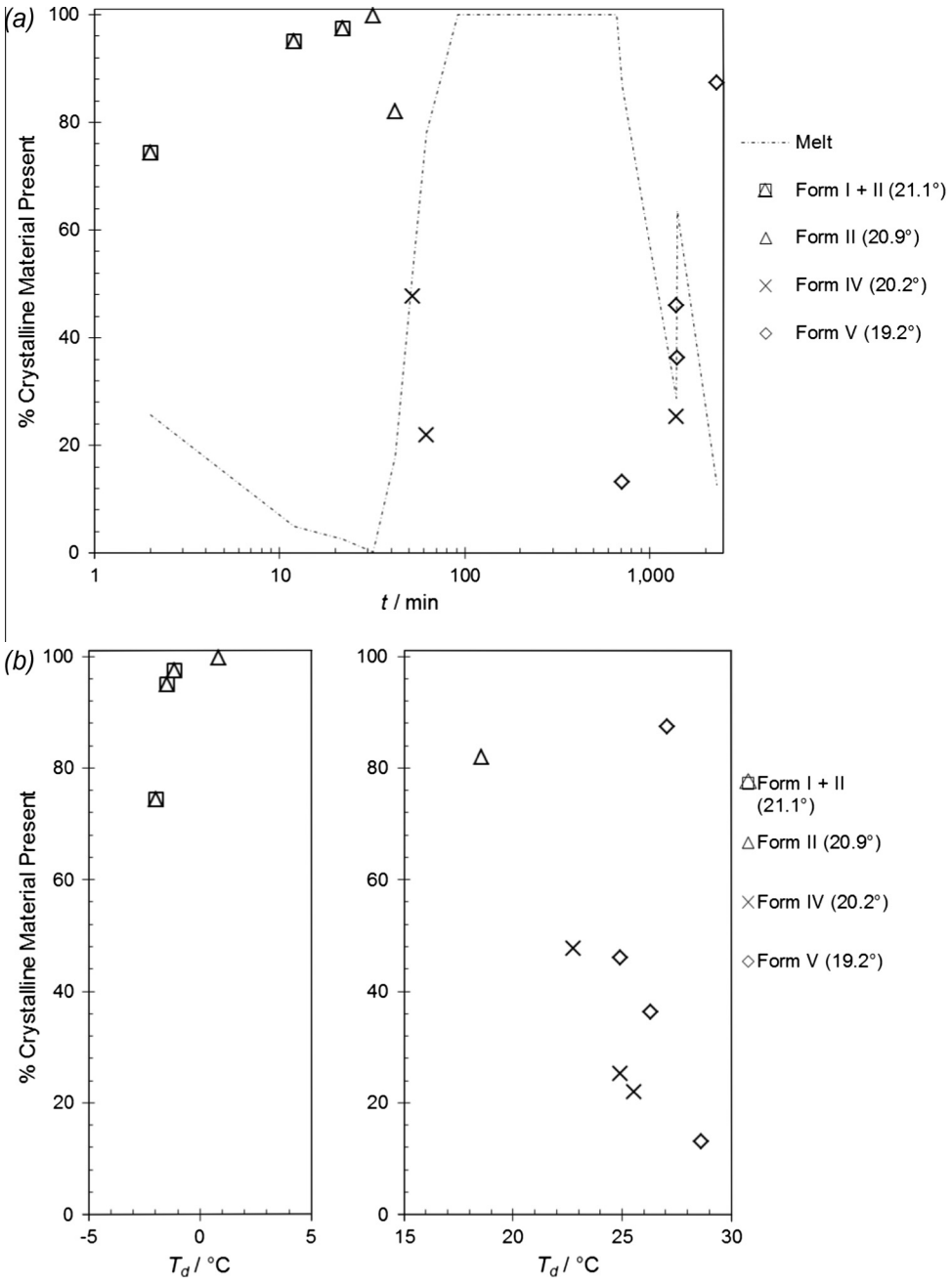

Fig. 14. Percentage of crystalline material present plotted against (a) time and (b) droplet temperature.

constructed. Fig. 15 shows the results from the droplet in Fig. 13 presented in this format alongside the van Malssen et al. boundaries.

The transformations observed up to Form IV are reasonably consistent with the van Malssen et al. scheme. However, Form V is observed at a higher temperature, and earlier than the van Malssen et al. scheme. This difference could be due to differences in composition (origin) of the cocoa butters and the thermal history of the sample (*e.g.* being warmed from a colder temperature). The Côte d'Ivoire droplets experienced significantly faster initial cooling rates and were subject to varying temperatures and phase transitions.

This difference may be due to the low Biot number in the droplet (as suggested by Pore et al. (2009)). A low Biot number indicates a nearly uniform temperature distribution within the droplet, which together with rapid cooling at 130 K/min will result in the formation of a large quantity of small sized Forms I and II crystals. With a larger bulk sample, the Biot number will be larger and nucleation is more likely to occur at the cold interface, giving a small number of large crystals. On warming, any Form I rapidly transforms into Form II. As the droplet is warmed further, Form II quickly transforms into Form IV. This rapid transformation is attributed to the collapse of the vertical chain Form II configuration to the herringbone Forms III/IV structure with alternating parallel rows which occurs unhindered (Larsson, 1966) as quoted in Kellens et al. (1991)). In terms of the droplet, this will mean that there will be a large number of Forms III/IV crystals formed which are all small in size. As the Forms IV to V transition is diffusion controlled and involves a complete reordering of every row of the Form IV structure (Kellens et al., 1991), having small Form IV crystals will help speed up this process by (*i*) Form IV melting quickly, and (*ii*) increased number of Form V nucleation sites. It is also possible that the initial rapid cooling results in the nucleation of all Forms. On warming, the large number of small sized lower melting polymorph crystals melts and allow the higher melting polymorphs (Forms IV and V) to grow via a process of Ostwald ripening.

The effect of temperature history and composition is the subject of ongoing work with the SDFA, exploiting its capacity to control the temperature history directly and to characterise the polymorphs present *in situ* and in real time.

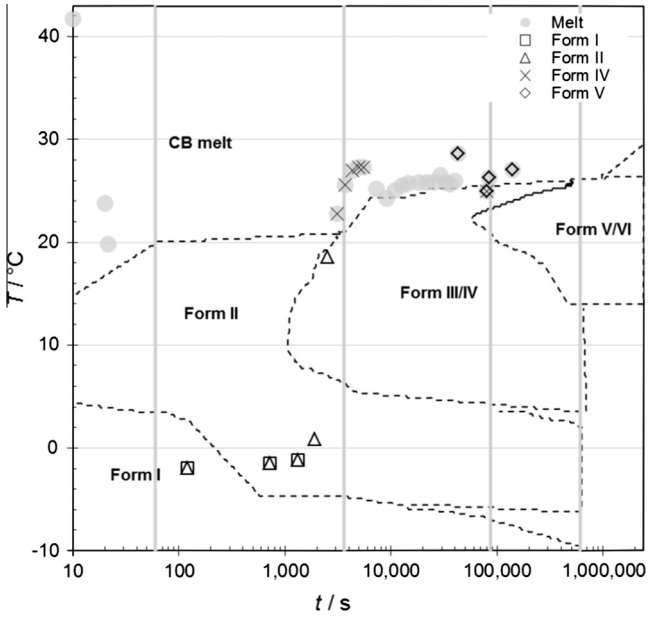

Fig. 15. Thermal trajectory and polymorphic forms observed for the droplet in Fig. 12 plotted on a phase transition map. The dashed lines show the phase transition boundaries reported by Van Malssen et al. (1999) for isothermal testing of a Cameroon CB.

5. Conclusions

The single droplet freezing apparatus (SDFA) has been optimised for studying crystallisation in droplets. It is able to offer very fast cooling rates, up to 200 K/min for the droplet sizes studied here, and allows real time observation of the evolving crystalline structure in cocoa butter droplets. Video microscopy has been used to monitor the different stages of freezing. A droplet freezing study using an Ivory Coast CB showed that phase change at the droplet thermocouple, T_d, lags behind nucleation at the base of the droplet. Numerical simulation of the cooling of the droplet showed that this lag is due to the non-uniform internal temperature distribution of the droplet, which is a result of the non-uniform local heat transfer coefficient across the surface of the droplet. These results showed that the freezing process cannot be described reliably by a 1D inward freezing shell model.

A second droplet freezing experiment, in which the droplet was subjected to temperature changes over extended time, showed that phase transformations in the droplet were similar to those in the van Malssen et al. isothermal phase transition scheme (Van Malssen et al., 1999). However, Form V was observed early in the droplet which could be due to the difference in thermal history or composition between their material and the one studied here.

Acknowledgements

The provision of an EPSRC studentship for AMT and project support from Nestlé PTC York is gratefully acknowledged. The apparatus was constructed by Lee Pratt, Gary Chapman, Kevin Swan and Wei-Yao Ma. Assistance with the DSC testing from Zlatko Saraçevic, video microscopy from Dr Simon Butler, and general X-ray analysis from Dr Joanna Stasiak are all gratefully acknowledged.

References

Beckett, S.T., 2009. Useful physical constants. In: Industrial Chocolate Manufacture and Use. Blackwell Publishing, pp. 667–668.
Clarkson, E., Clarkson, C.E., Malkin, T.J., 1934. Alternation in long-chain compounds. Part II. An X-ray and thermal investigation of the triglycerides. J. Chem. Soc., 666–671
Cullity, B.D., 1956. Elements of X-ray Diffraction. Addison-Wesley Publishing Company Inc, Massachusetts.
D'Souza, V., DeMan, J.M., DeMan, L., 1990. Short spacings and polymorphic forms of natural and commercial solid fats: a review. J. Am. Oil Chem. Soc. 67, 835–843.
Fessas, D., Signorelli, M., Schiraldi, A., 2005. Polymorphous transitions in cocoa butter, a quantitative study. J. Therm. Anal. Calorim. 82, 691–702.
Fuchs, N.A., 1959. Evaporation and Droplet Growth in Gaseous Media. Pergamon Press Ltd, London.
Galloway, S.J., Smyth, N.F., 1997. A numerical method for predicting crystal microstructure. Appl. Math. Model. 21, 569–578.
Gwie, C.G., Griffiths, R.J., Cooney, D.T., Johns, M.L., Wilson, D.I., 2006. Microstructures formed by spray freezing of food fats. J. Am. Oil Chem. Soc. 83, 1053–1062.
Hindmarsh, J.P., Russell, A.B., Chen, X.D., 2003. Experimental and numerical analysis of the temperature transition of a suspended freezing water droplet. Int. J. Heat Mass Transfer 46, 1199–1213.
Hindmarsh, J.P., Hollingsworth, K.G., Wilson, D.I., Johns, M.L., 2004. An NMR study of the freezing of emulsion-containing drops. J. Colloid Interface Sci. 275, 165–171.
Hindmarsh, J.P., Russell, A.B., Chen, X.D., 2007. Fundamentals of the spray freezing of foods—microstructure of frozen droplets. J. Food Eng. 78, 136–150.
Hirasawa, S., Kawanami, T., Kinoshita, T., Watanabe, T., Atarashi, T., 2012. Numerical analysis of forced convection heat transfer around spherical particles packed in fluid flow. J. Phys. Conf. Ser. 395, 012143.
Huang, T.C., Toraya, H., Blanton, T.N., Wu, Y., 1993. X-ray powder diffraction analysis of silver behenate, a possible low-angle diffraction standard. J. Appl. Crystallogr. 26, 180–184.
Incropera, F.P., DeWitt, D.P., Bergman, T.L., Lavine, A.S., 2007. Fundamentals of Heat and Mass transfer. John Wiley & Sons.
Johnson, T.A., Patel, V.C., 1999. Flow past a sphere up to a Reynolds number of 300. J. Fluid Mech. 378, 19–70.

Kay, J.M., Nedderman, R.M., 1974. An Introduction to Fluid Mechanics and Heat Transfer with Applications in Chemical & Mechanical Process Engineering. Cambridge University Press, Cambridge.
Kellens, M., Meeussen, W., Gehrke, R., Reynaers, H., 1991. Synchrotron radiation investigations of the polymorphic transitions of saturated monoacid triglycerides. Part 1: Tripalmitin and tristearin. Chem. Phys. Lipids 58, 131–144.
Larsson, K., 1966. Classification of glyceride crystal forms. ACTA Chem Scand. 20, 2255–2260.
Lopez, C., Ollivon, M., 2009. Crystallisation of triacylglycerols in nanoparticles. J. Therm. Anal. Calorim. 98, 29–37.
Macleod, C.S., McKittrick, J.A., Hindmarsh, J.P., Johns, M.L., Wilson, D.I., 2006. Fundamentals of spray freezing of instant coffee. J. Food Eng. 74, 451–461.
Macmillan, S.D., Roberts, K.J., 2002. In situ small angle X-ray scattering (SAXS) studies of polymorphism with the associated crystallization of cocoa butter fat using shearing conditions. Cryst. Growth Des. 2, 221–226.
Macmillan, S.D., Peacock, C.A., Roberts, K., Rossi, A., Wells, M.A. Smith, I.H. 2002. In: In Situ XRD Studies of Cocoa Butter Fat Under Thermal Processing and Shearing Conditions Lipid Structural Properties Symposium.
Pore, M., Seah, H.H., Glover, J.W.H., Holmes, D.J., Johns, M.L., Wilson, D.I., Moggridge, G.D., 2009. In-situ X-ray studies of cocoa butter droplets undergoing simulated spray freezing. J. Am. Oil Chem. Soc. 86, 215–225.
Ranz, W.E., Marshall, W.R., 1952. Evaporation from drops Part I. Chem. Eng. Prog. 48, 141–146.
Schlichter Aronhime, J., Sarig, S., Garti, N., 1988. Reconsideration of polymorphic transformations in cocoa butter using the DSC. J. Am. Oil Chem. Soc. 65, 1140–1143.
Sonwai, S. 2002. The Effect of Shear on Crystallisation of Cocoa Butter. Ph.D. Dissertation, University of Cambridge.
Spigno, G., Pagella, C., De Faveri, D.M., 2001. DSC characterisation of cocoa butter polymorphs. Ital. J. Food Sci. 13 (275-28).
Tanner, F.X., 2011. Droplet freezing and solidification. In: Ashgriz, N. (Ed.), Handbook of Atomization and Sprays Theory and Applications. Springer, New York, pp. 327–338.
Turton, R., Levenspiel, 1986. A short note on the drag correlation for spheres. Powder Technol. 47, 83–86.
Ueno, S., Minato, a., Yano, J., Sato, K., 1999. Synchrotron radiation X-ray diffraction study of polymorphic crystallization of SOS from liquid phase. J. Cryst. Growth 198–199, 1326–1329.
Van Langevelde, A., Driessen, R., Molleman, W., Peschar, R., Schenk, H., 2001. Cocoa-butter long spacings and the memory effect. J. Am. Oil Chem. Soc. 78, 911–918.
Van Langevelde, A., van Malssen, K., Peschar, R., Schenk, H., 2001. Effect of temperature on recrystallization behavior of cocoa butter. J. Am. Oil Chem. Soc. 78, 919–925.
Van Malssen, K., Peschar, R., Brito, C., Schenk, H., 1996. Real-time X-ray powder diffraction investigations on cocoa butter. III. Direct beta-crystallization of cocoa butter: occurrence of a memory effect. J. Am. Oil Chem. Soc. 73, 1225–1230.
Van Malssen, K., Peschar, R., Schenk, H., 1996a. Real-time X-ray powder diffraction investigations on cocoa butter. I. Temperature-dependent crystallization behavior. J. Am. Oil Chem. Soc. 73, 1209–1215.
Van Malssen, K., Peschar, R., Schenk, H., 1996b. Real-time X-ray powder diffraction investigations on cocoa butter. II. The relationship between melting behavior and composition of beta-cocoa butter. J. Am. Oil Chem. Soc. 73, 1217–1223.
Van Malssen, K., van Langevelde, A., Peschar, R., Schenk, H., 1999. Phase behavior and extended phase scheme of static cocoa butter investigated with real-time X-ray powder diffraction. J. Am. Oil Chem. Soc. 76, 669–676.
Wille, R.L., Lutton, E.S., 1966. Polymorphism of cocoa butter. J. Am. Oil Chem. Soc. 43, 491–496.